

Selenide Heterostructure Nanosheets with Efficient Near-Infrared Photothermal Conversion for Therapy

Yanbang Lian, Congcong Wang, Yu Meng, Junqiang Dong, Jianbin Zhang, Shiqing Xu, Gongxun Bai,* and Jianbo Gao*



Cite This: *ACS Omega* 2023, 8, 9371–9378



Read Online

ACCESS |



Metrics & More

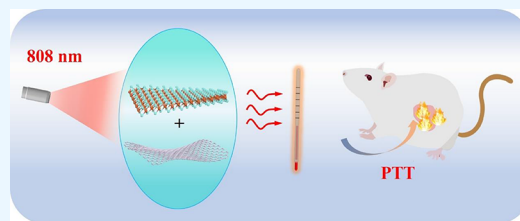


Article Recommendations



Supporting Information

ABSTRACT: Photothermal therapy has been regarded as one of promising ways for tumor treatment. However, nanoagents with highly efficient thermal conversion and good bio-compatibility are still needed to be developed in biomedicine. In this work, we prepared two-dimensional heterostructures with bismuth selenide and tungsten selenide nanosheets as photothermal nanoagents. Near-infrared photothermal conversion of selenide heterostructure nanosheets can reach up to 40.75% under 808 nm excitation. It is known that selenium is a critical element to human health. More importantly, our experiments with mice show that the heterostructure nanosheets have low toxicity and high biocompatibility both in vitro and in vivo. The nanoagents based on heterostructures can effectively realize photothermal tumor ablation. It is suggested that the developed selenide nanosheets have great potential application in cancer therapy.



1. INTRODUCTION

With increasing development of nanomaterials, numerous therapeutic methods are emerging for efficient cancer treatments, including photothermal therapy, drug release therapy, photoacoustic imaging, photodynamic therapy, and near-infrared infrared imaging.^{1–4} In particular, photothermal therapy can utilize suitable nanomaterials to convert light energy into heat energy, resulting in tumor thermal ablation and cell necrosis.^{5–7} Compared with traditional methods, photothermal therapy has advantages of high targeting, low adverse effects, and repeatable treatment.^{8,9} It is noted that during photothermal therapy, an appropriate temperature of the tumor ablation site must be maintained, which requires photothermal materials with high photothermal conversion efficiency and stability.^{10–12} Hence, it is greatly important to develop theranostic nanoagents that have high photothermal conversion and good bio-compatible abilities for effective cancer therapy.

In recent years, two-dimensional nanomaterials have attracted considerable attention in biomedicine, owing to their optical absorption, large surface area, photoluminescence, intriguing electrical properties, and high wear resistance.¹³ Hence, there are numerous current two-dimensional nanosheets used as photothermal nanoagents for cancer therapy.^{14–16} Nevertheless, some challenging issues in two-dimensional nanomaterials remain to be resolute before clinical use.¹⁷ On the one hand, short-term and long-term biosafety is an absolute qualification for biomedicine.^{18–20} Biodegradability and stability are very significant in clinical development. Thus, toxic elements cannot be considered and

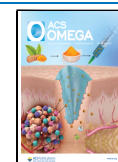
some necessary elements can be considered for animals.²¹ On the other hand, theranostic nanoagents with high photothermal conversion are greatly desired under near-infrared excitation,^{22,23} as the near-infrared light within the biological window can effectively penetrate the biological tissue.^{13,24} However, the reported two-dimensional nanomaterials display several degrees of inadequacies for cancer treatment.²¹ For instance, carbon-based graphene and reduced graphene oxide have low efficiency of light-to-heat conversion, leading to poor beneficial abilities and compensatory high dosage.²⁵ Black phosphorus uncertainty has both compensations and drawbacks for therapeutic development, such as complications of preparation and storing.²⁶ On the other hand, for two-dimensional antimonene nanomaterials, their instability would lead to toxicity in water.²⁷ According to vital medical requirements for clinical development, we have prepared selenide-based anticancer treatment using bismuth and tungsten selenide-made nanomaterials.

Selenium (Se), as a member of the chalcogen family, is an important element to animal health.¹⁴ In the past years, various selenide nanostructures have been fabricated for optoelectronic applications.²⁹ Our recent report has suggested that MoSe₂:Er can be used in photothermal therapy.²⁸ However, only few

Received: December 14, 2022

Accepted: February 22, 2023

Published: March 3, 2023



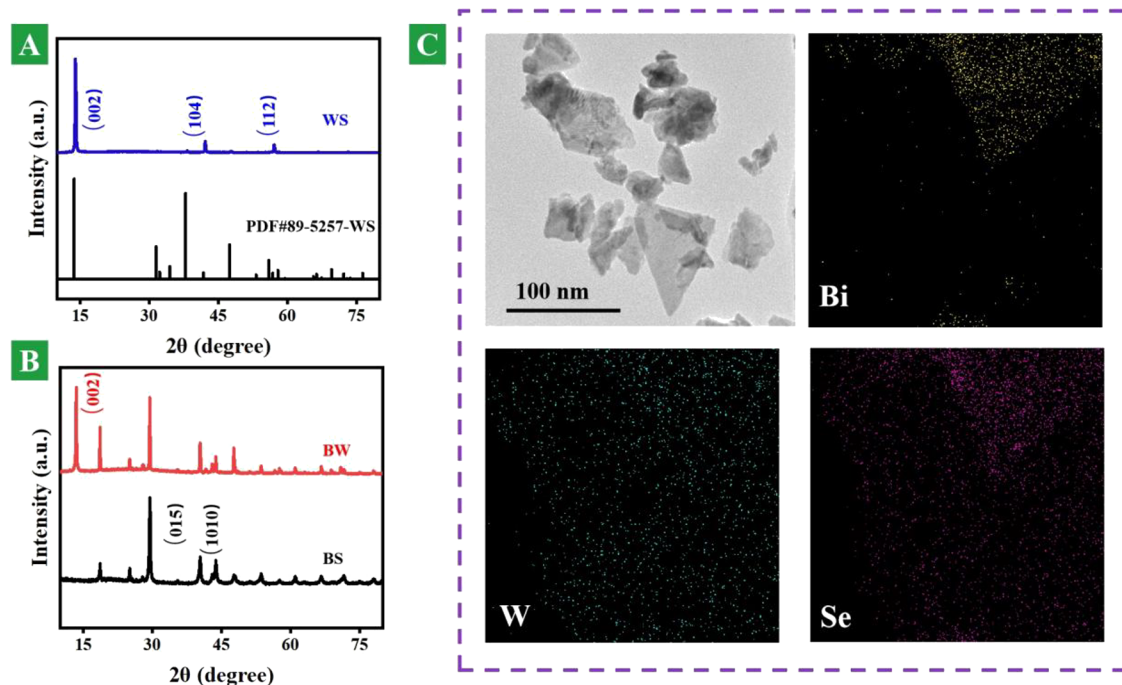


Figure 1. Morphology and structure. (A) XRD patterns of WS nanosheets and standard card (PDF #89-5257). (B) XRD patterns of BS and BW heterostructure nanosheets. (C) HR-TEM image of BW heterostructure nanosheets and energy-dispersive mapping images of Bi, W, and Se in BW heterostructure nanosheets.

studies on selenide-made nanomaterials have been reported in the biomedical field. In this work, two dimensional heterostructure nanosheets are constructed with Bi_2Se_3 (BS) and WSe_2 (WS) nanosheets. The heterostructure bismuth selenide and tungsten selenide (BW) nanosheets are designed to enhance light absorption and heat localization,³⁰ in order to realize better properties. The newly prepared selenide-based nanosheets were stable and biocompatible with antitumor effects. Our results show anticancer efficacy of developed selenide nanosheets, beneficial mechanisms, and their impact on modification of the tumor microenvironment.

2. EXPERIMENTAL SECTION

2.1. Synthesis of Heterostructure Nanosheets. The WS (99.99%) and BS (99.99%) powders were purchased from Changsha Tianjiu Metal Material Co., Ltd. $\text{C}_5\text{H}_9\text{NO}$ (99.5%) and polyvinyl pyrrolidone (PVP) were purchased from Shanghai Aladdin Technology Co., Ltd. The mixed powders (1 g) of WS and BS were weighed according to the atomic ratio (W:Bi = 1:1). Then, the above powder was put into an agate mortar with 5 mL of 1-methyl-2-pyrrolidinone (NMP) and ground for 30 min. The suspension was dispersed into 100 mL of NMP for probe ultrasound (900 W, 30%) stripping for 48 h. Finally, the heterostructure nanosheets named BW were obtained after centrifugation at 6000 rpm for 5 min. The surface of BW nanomaterials was medicated with PVP to improve biocompatibility. 20 mg BW nanoparticles were dispersed in 5 mL of deionized water and 50 mg of PVP. After water bath ultrasound, centrifuging, and washing, the modified BW nanosheets were redistributed into deionized water.

2.2. Characterization. An X-ray powder diffractometer (XRD, D2 PHASER, Bruker) with $\text{Cu K}\alpha$ ($\lambda = 0.15406$ nm) was utilized to record X-ray diffraction data for studying crystalline phases. A high-resolution transition electron microscope (HR-TEM, JEM-2100, JEOL) was used to study micro

morphology structures. Chemical and elemental compositions were studied by a Thermo Scientific K-Alpha photoelectron spectrometer. The temperature changes were controlled by an 808 nm laser and observed by a UT 325 thermometer. The infrared thermal pictures were taken by a FLIR One Pro infrared camera.

2.3. Cell Culture. Human KYSE150 esophageal squamous cells were purchased from Procell (Wuhan, China). The cells were maintained in RPMI 1640 medium (Biological Industries, Israel) supplemented with 10% fetal bovine serum (Biological Industries, Israel) containing 100 U/mL penicillin and 100 g/mL streptomycin at 37 °C with 5% CO_2 .

2.4. Cell Toxicity Assay. The MTT assay was used to evaluate the biocompatibility with the KYSE150 cells (esophageal cancer cells). After the cells were seeded in 96-well plates at a density of five cells/well for 24 h, the cells were treated with 200 μL of medium containing the PVP or BW nanosheets of different concentrations ranging from 10 to 100 ppm for 48 h. After that, the cells were stained with 0.5 mg/mL of MTT for 4 h and the formed formazan was dissolved with 150 μL of DMSO. Then, the absorbance at 490 nm of the wells was measured by a microplate reader (Spark, Tecan, Switzerland).

2.5. Cell Viability Detection. The cell viability was detected by Live & Dead Viability/Cytotoxicity Assay Kit (Meilunbio, Dalian, China) according to the manufacturer's instruction. This two-color viability assay based on membrane integrity and esterase activity, and the live cells were stained with Calcein AM (green) and dead cells with PI (red). Briefly, the well-growing KYSE150 cells were harvested and seeded in a 24-well plate at a density of 2×10^5 . After 24 h, the cells were treated with BW nanosheets or PVP solutions (50 ppm) and cultured for another 24 h. Finally, the cells were labeled with Calcein AM and PI staining solutions at 37 °C for 4 h and the

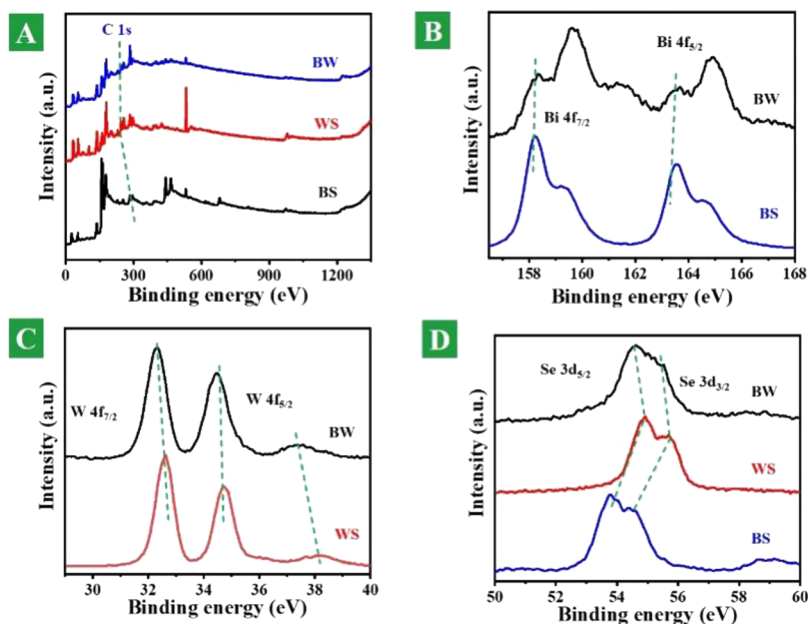


Figure 2. Elemental composition and valence states. (A) Survey XPS spectra of full elements of fabricated BS, WS, and BW heterostructure nanosheets. (B) XPS spectra of Bi 4f in BS and BW heterostructure nanosheets. (C) XPS spectra of W 4f in BS and BW heterostructure nanosheets. (D) XPS spectra of Se 3d in BS and BW heterostructure nanosheets.

Live & Dead cells were detected by an inverted fluorescence microscope (DMI8, Leica, Germany).

2.6. Assessment of In Vitro Toxicity. Animals' experiments protocols were approved by the Animal Care and Use Committee of Zhengzhou University Laboratory Animal Center, and the in vivo experiments were carried out in accordance with the approved guidelines. SCID female mice (6–8 weeks old, 18–20 g) were purchased from the Zhengzhou University Laboratory Animal Center, and the mice were housed in an independent ventilated cage in a specific pathogen-free environment with a temperature of 23 ± 1 °C, humidity of 50–60%, and 12 h of light followed by 12 h of darkness per day. The mice were injected intravenously with 0.2 mL of PVP and BW nanosheets at a concentration of 2 mg/mL and then monitored carefully for 0, 1, 2, and 4 weeks. The pathological features of internal organs including heart, liver, kidney, spleen, and muscle were examined by hematoxylin and eosin (H&E) staining.

2.7. In Vitro Photothermal Experiments. To evaluate the photothermal cytotoxicity induced by irradiation source, the KYSE150 cells were seeded into a 96-well plate ($\approx 5 \times 10^3$ cells/well) and incubated for 24 h and then co-cultivated with PVP and BW (0.2 mL, $1 \text{ mg}\cdot\text{mL}^{-1}$), respectively. Irradiated with the 808 nm laser at a power density of $0.6 \text{ W}\cdot\text{cm}^{-2}$ for different periods of time (up to 5 min) and cultured for another 24 h, the cells were labeled with Calcein AM and PI staining solutions at 37 °C for 4 h, and finally the Live & Dead cells were detected by an inverted fluorescence microscope (DMI8, Leica, Germany).

2.8. In Vivo Photothermal Experiments. SCID mice (5–6 weeks old) were subcutaneously injected with KYSE150 cells (1×10^7 cells in 100 μL of phosphate-buffered saline (PBS)) in the right flank to establish the tumor-bearing mouse model. When the volume of tumors reached about 350 mm^3 , the mice were separated into the corresponding saline (negative control) group, PVP membrane group, and BW group. As shown in Figures S1 and S2, after anesthesia with

isoflurane, totally 0.2 mL of various reagents ($1 \text{ mg}\cdot\text{mL}^{-1}$) was homogeneously injected in the tumor in situ. After laser illumination (808 nm, $0.6 \text{ W}\cdot\text{cm}^{-2}$) for 5 min, The corresponding temperature changes of the tumors after NIR irradiation were recorded by a photothermal camera. The tumor size and body weight were measured every other day. At the end of the experiment, the mice were euthanized and the tumors were isolated, weighed, photographed, and fixed with 10% formalin solution.

3. RESULTS AND DISCUSSION

The crystal structure plays a key role in material properties. An X-ray diffraction (XRD) pattern can be used for studying phases and structures. Figure 1A shows XRD patterns of WS nanosheets and the standard card (PDF #89-5257) of WS. Compared with the standard card of the bulk phase, it is seen that after ultrasound, the (002) peak of WS nanosheets is very prominent and the other peaks become weakened or even disappear. This is mainly due to the optimal orientation of the material after ultrasound.²⁸ Figure 1B indicates that the prepared BW nanosheets are composed of two-dimensional BS and WS nanosheets with around 100 nm plane size. The smaller two-dimensional nanosheets can move inside the body to different organs.^{18–20} Figure 1C shows HE-TEM and elemental mapping images of BW heterojunction nanosheets. It is well seen in a relatively flat sheet structure and its stacking. The elemental distribution of Bi, W, and Se can be well observed. Both Bi and W elements have strong X-ray attenuation ability, which is suitable for computed tomography imaging. We can see that the large slice layer of the base is WS nanosheets and the attached slice layer is the BS nanosheet. Figure S3 also confirms layered heterojunction composites consisting of BS and WS nanosheets with around 100 nm plane size. These images indicate the chemical elemental composition and microstructure of the heterojunction nanosheets.

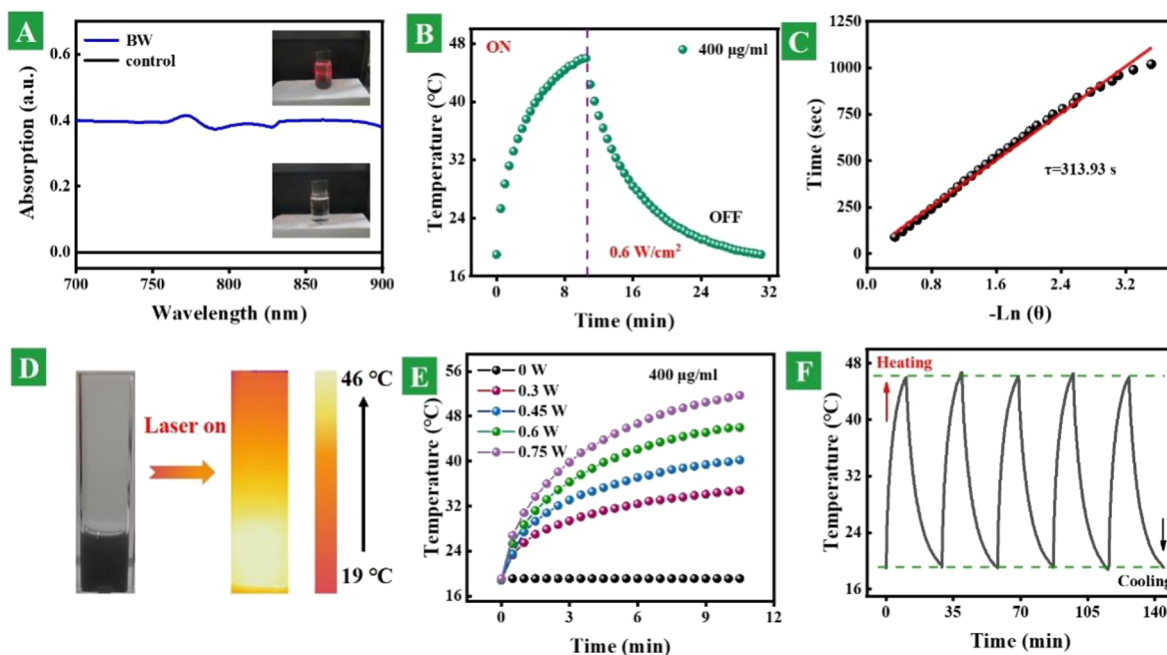


Figure 3. Photothermal conversion properties. (A) Absorption spectra of BW heterostructure nanosheets and control samples. The inset pictures are corresponding samples under excitation of the 808 nm laser. (B) Whole thermal profile with the function of excitation time of 0.4 mg/mL of BW heterostructure nanosheet dispersion under 0.6 W/cm² power density. (C) Time constant attained from the sample cooling procedure. (D) Optical and photothermal images of the 0.4 mg/mL BW heterostructure nanosheet solution under 808 nm laser excitation. (E) Power-dependent photothermal performance of the 0.4 mg/mL BW heterostructure nanosheet solution under the power changing from 0 to 0.75 W. (F) Thermal performance of the BW heterostructure nanosheet dispersion in five heating and cooling cycles.

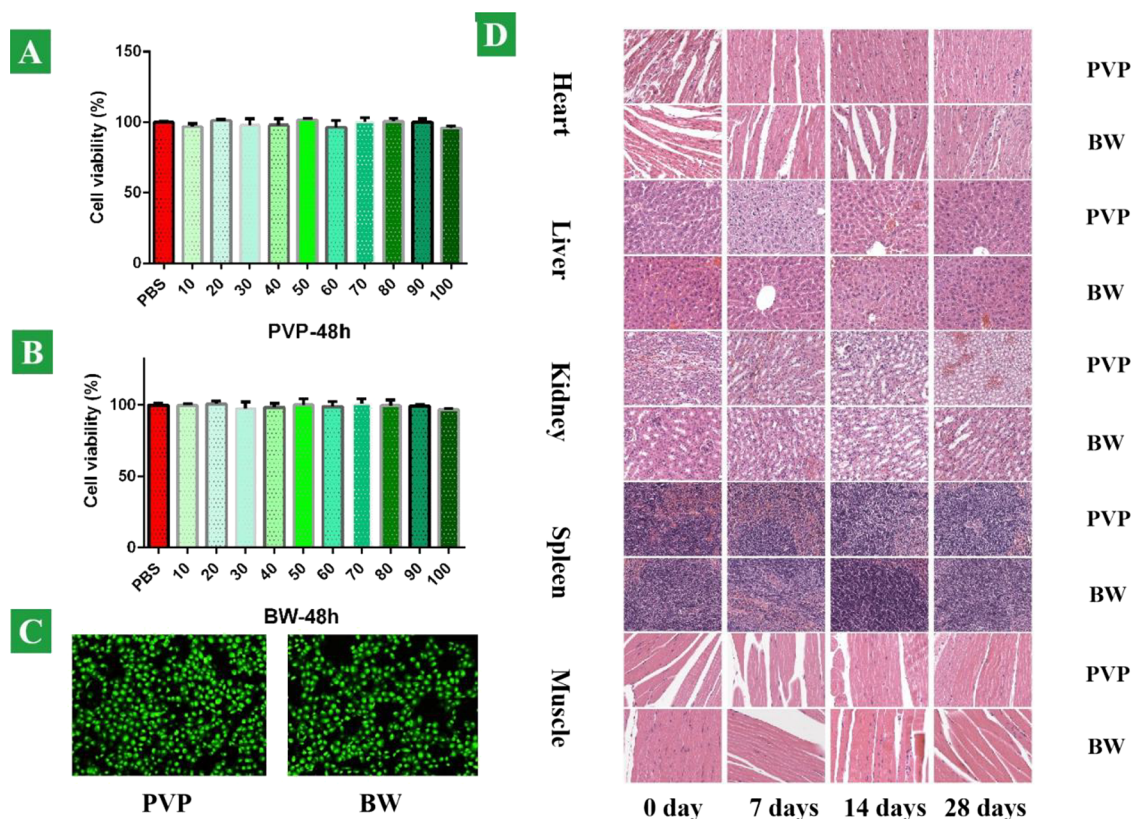


Figure 4. Biocompatibility and biosafety evaluation. Relative cell viability of KYSE150 cells cultivated for 48 h with various concentrations: (A) PVP and (B) BW nanosheets. (C) Fluorescence images of KYSE150 cells stained by Calcine AM/PI in the copresence of the PVP and BW nanosheets, respectively. (D) Pathological HE staining of SCID mouse organs such as heart, liver, kidney, spleen, and muscle tissue at 0, 7, 14, and 28 days.

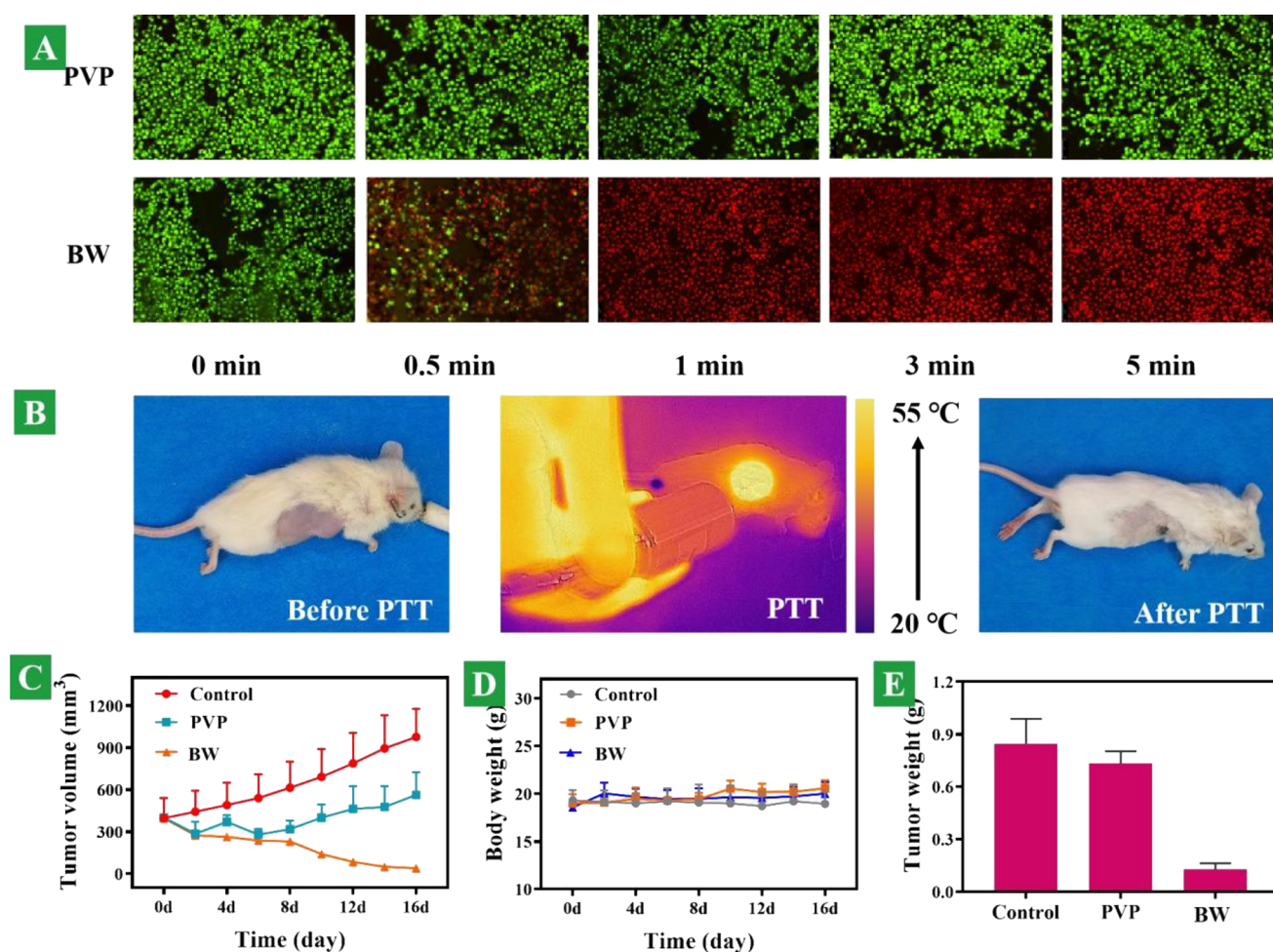


Figure 5. In vitro and in vivo photothermal performance. (A) Fluorescence images of KYSE150 cells stained with Calcine AM/PI in the copresence of the PVP and BW nanosheets, respectively, combined with 808 nm laser irradiation. (B) Images of tumor sites injected intratumorally with BW nanosheets with 808 nm excitation, before and after PTT (photothermal therapy). (C) Tumor growth curves of mice treated with different groups: PBS, PVP, and BW during 16 days. (D) Body weight variation of mice corresponding to various groups. (E) Ultimate tumor weight after different treatments in 16 days.

Photoelectron spectroscopy can well reflect the chemical environment of the elements and provide evidence for the synthesis of designed materials. Figure 2A shows the XPS spectra of the whole element. Figure 2B shows the XPS spectra of Bi 4f in the BS and BW heterostructure nanosheets. In the Bi element spectra, there are four peaks contributing to orbital Bi 4f_{7/2}, Bi 4f_{5/2} and BiO_x 4f_{7/2}, and BiO_x 4f_{5/2}, which exhibit the interaction of Bi elements with oxygen elements.²⁸ Their values are 158.33, 175.13, 159.63, and 164.96 eV in the BW nanomaterials and are 158.23, 163.58, 159.28, and 164.63 eV in pure BS. They are offset by 0.1, 0.1, 0.38, and 0.33 eV, respectively. Figure 2C shows the XPS spectra of W 4f in the BS and BW heterostructure nanosheets. In the W elemental spectra, there are two main peaks corresponding to W 4f_{7/2} and W 4f_{5/2}, respectively. In BW nanomaterials, the values are 32.33 and 34.48/37.43 eV, and in pure WS, they are 32.33 and 34.48/37.43 eV, and they are offset by 0.3, 0.2, and 0.77 eV, respectively. Figure 2D shows the XPS spectra of Se 3d in the BS and BW heterostructure nanosheets. In the Se elemental spectrum, it has two important contribution tracks Se 3d_{3/2} and Se 3d_{5/2}. In BW nanomaterials, the values are 54.63 and 55.53 eV, and in pure WS, they are 54.93 and 55.68 eV, and they are offset by 0.3 and 0.15 eV, respectively. The above changes indicate that the material is not a simple physical

mixture but also an interaction with electron transfer between the two nanomaterials. The successful preparation of the BW heterostructure nanosheets is illustrated in our preparation.

In order to evaluate the photothermal conversion properties, the absorption and photothermal performances were recorded. Figure 3A shows the absorption spectra of the BW heterostructure nanosheets and control samples. The absorption of the BW nanosheet solution is much higher than that of the blank solution. The inset picture of the BW sample shows the Tyndall effect under excitation of the 808 nm laser. Figure 3B shows a whole thermal profile with the function of excitation time of 0.4 mg/mL BW heterostructure nanosheet dispersion under 0.6 W/cm² power density. On the basis of temperature changes in the cooling process, the essential time constant can be deduced, as shown in Figure 3C. The photothermal conversion efficiency is premeditated to be 40.75% according to previous reports. Figure 3D displays the optical and photothermal images of the 0.4 mg/mL BW heterostructure nanosheet solution under 808 nm laser excitation, and the excitation power is 0.6 W/cm². Figure 3E shows the power-dependent photothermal performance of the 0.4 mg/mL BW heterostructure nanosheet solution under the power changing from 0 to 0.75 W. Figure 3F presents the thermal performance of BW heterostructure nanosheet

dispersion in five heating and cooling cycles. The results suggest that the prepared heterostructure nanosheets have good photothermal conversion and chemical stability.

We examined the potential cytotoxicity of the BW heterostructure nanosheets toward cancer cells *in vivo* and *in vitro*, with PVP as the control group. The relative viability of the KYSE150 cells (esophageal cancer cells) was determined by the MTT assay. Cancer cells were incubated with BW nanosheets and PVP at various concentrations of 10, 20, 30, 40, 50, 60, 70, 80, 90, and 100 ppm to observe their effects on cell viability. As shown in Figure 4A,B, no significant cytotoxicity was detected from the BW nanosheets and PVP, demonstrating that the heterostructure nanosheet does not compromise the biocompatibility. For *in vivo* monitoring of the biosafety, there was no dead cancer cell stained as red color, which is shown in Figure 4C. To further assess the possible toxicity of the BW heterostructure nanosheets *in vivo*, both BW nanosheets and PVP were systematically investigated after intravenous injection into the SCID mice (6–8 weeks old, ~20 g). The mice injected with the PVP and BW heterostructure nanosheets were monitored carefully to observe the long-term toxicity of the BW heterostructure nanosheets. Neither death nor obvious toxicity was observed at a specific time. Mice were sacrificed after injection on 0, 7, 14, and 28 days, and organs such as heart, liver, kidney, spleen, and muscle were sliced and stained with H&E for histology analysis. No organ damage or inflammatory lesion was observed from the organs, and negligible histopathological abnormalities or lesions observed from both treated groups bode well for the application of the BW heterostructure nanosheets *in vivo* (Figure 4D). There was no material deposition in the cells and no obvious cell apoptosis and necrosis.

Photothermal therapy of cancer cells is shown in Figure 5A. After 30 s of laser exposure, the temperature rapidly reached 50.2 °C and a vast majority of cancer cells died and were stained with PI with bright red fluorescence in the BW group, whereas all of the cancer cells stayed alive in the PVP group and stained with Calcein AM with green fluorescence. On the basis of our results, irradiation with the 808 nm laser at 0.6 W/cm² for 5 min is sufficient to kill cancer cells. This indicates that the photothermal treatment effect of the BW on tumor cells is excellent and poses a unique advantage in clinical applications because this photothermal system can modulate the therapeutic effects externally by simply altering the irradiation time.

The *in vivo* therapeutic efficacy of the BW was evaluated in an *in situ* established tumor model by subcutaneous injection of KYSE150 esophageal cancer cells into the right front flank of the SCID mice. When the volume of tumors reached approximately 350 mm³, the mice were separated into three groups as mentioned above. For comparison, the mice treated with phosphate buffer saline solutions (PBS) served as the control, and mice treated with PVP served as the control. For *in vivo* monitoring of the photothermal effects, the infrared thermographic maps and the maximum temperature of 54.8 °C were measured simultaneously by using an infrared thermal imaging camera, as shown in Figure 5B. After NIR irradiation, the mice in the different experimental groups were monitored for signs of distress daily, and the tumor volume was measured every 2 days. Neither death nor obvious toxicity such as abnormal body weight, drinking, or eating was observed during the post-therapy period. The variation in the tumor volume

was consistent with that of the treatment. As shown in Figure 5C, the tumors in the BW group dwindled gradually after NIR irradiation. The tumor-bearing mice after the BW and NIR treatments can survive for over 14 days without a single death. In contrast, tumor inhibition cannot be observed from the control groups of PBS and PVP. These results corroborate the excellent efficacy of BW in photothermal cancer therapy *in vivo*. Meanwhile, no remarkable changes in mouse weight occurred throughout the tumor-growing period. The overall mouse mass fluctuated within the reasonable range, as shown in Figure 5D. After *in vivo* photothermal treatment on the tumor sites, greatly contrasting the other two, the tumor volume of the BW nanosheet group presented an enormous attenuation without recurrence behaviors, as shown in Figure 5E. In contrast, tumor inhibition was not observed in the PBS and PVP groups, while all the mice lived for more than 2 weeks with the absence of body weight loss and death. These results corroborate the excellent efficacy of the BW nanosheets in photothermal cancer therapy *in vivo*.

4. CONCLUSIONS

In summary, two-dimensional heterostructures with bismuth selenide and tungsten selenide nanosheets have been prepared by the sonication-assisted liquid exfoliation technology method. The results of XRD, TEM, and XPS suggest that the prepared heterostructure nanosheets have a tiny size and atomical layered thickness. The near-infrared photothermal conversion of the fabricated selenide heterostructure nanosheets can reach up to 40.75% under 808 nm excitation. Moreover, Se is a critical element to human health. The biological experiments with mice show that the heterostructure nanosheets have low toxicity and high biocompatibility *in vivo*. Tumor growth and mouse weight were monitored with BW nanosheets and laser irradiation. The tumor was almost completely ablated without recurrence. Trials on the *in vitro* viability of KYSE150 cells cultivated with BW nanosheets and histological analysis of major organs and muscles in tumor-bearing mice both show desirable biocompatibility and low toxicity of the objective nanosheets, which scarcely induce functional damages and pathological changes. Our results suggest that selenide heterostructure nanosheets with good biocompatibility and high near-infrared photothermal conversion are perspective candidates for photothermal therapy.

■ ASSOCIATED CONTENT

Supporting Information

The Supporting Information is available free of charge at <https://pubs.acs.org/doi/10.1021/acsomega.2c07964>.

In vitro experiments with mice; *in vitro* experimental operations; HR-TEM images of BW heterostructure nanosheets and energy-dispersive mapping of Bi, W, and Se in BW heterostructure nanosheets (PDF)

■ AUTHOR INFORMATION

Corresponding Authors

Gongxun Bai – Key Laboratory of Rare Earth Optoelectronic Materials and Devices of Zhejiang Province, College of Optical and Electronic Technology, China Jiliang University, Hangzhou, Zhejiang 310018, China; orcid.org/0000-0002-4066-0359; Email: baigx@cjlu.edu.cn

Jianbo Gao – Radiology Department, The First Affiliated Hospital of Zhengzhou University, Zhengzhou, Henan 450052, China; Email: cjr.gaojianbo@vip.163.com

Authors

Yanbang Lian – Radiology Department, The First Affiliated Hospital of Zhengzhou University, Zhengzhou, Henan 450052, China

Congcong Wang – Key Laboratory of Rare Earth Optoelectronic Materials and Devices of Zhejiang Province, College of Optical and Electronic Technology, China Jiliang University, Hangzhou, Zhejiang 310018, China

Yu Meng – Oncology Department, The First Affiliated Hospital of Zhengzhou University, Zhengzhou, Henan 450052, China

Junqiang Dong – Radiology Department, The First Affiliated Hospital of Zhengzhou University, Zhengzhou, Henan 450052, China

Jianbin Zhang – Department of Medical Oncology, Zhejiang Provincial People's Hospital, Affiliated People's Hospital, Hangzhou Medical College, Hangzhou, Zhejiang 310014, China

Shiqing Xu – Key Laboratory of Rare Earth Optoelectronic Materials and Devices of Zhejiang Province, College of Optical and Electronic Technology, China Jiliang University, Hangzhou, Zhejiang 310018, China

Complete contact information is available at:

<https://pubs.acs.org/10.1021/acsomega.2c07964>

Notes

The authors declare no competing financial interest.

ACKNOWLEDGMENTS

This work was financed by the Henan Provincial Medical Science and Technique Key Project (SBGJ2020002064), Zhejiang Provincial Natural Science Foundation of China (LZ21E020004), and National Natural Science Foundation of China (6217032304).

REFERENCES

- (1) Yang, B.; Yao, H.; Tian, H.; Yu, Z.; Guo, Y.; Wang, Y.; Yang, J.; Chen, C.; Shi, J. Intratumoral synthesis of nano-metalchelate for tumor catalytic therapy by ligand field-enhanced coordination. *Nat. Commun.* **2021**, *12*, 3393.
- (2) Gao, P.; Chen, Y.; Pan, W.; Li, N.; Liu, Z.; Tang, B. Antitumor agents based on metal-organic frameworks. *Angew. Chem., Int. Ed.* **2021**, *60*, 16763–16776.
- (3) Dong, L.; Sun, L.; Li, W.; Jiang, Y.; Zhan, Y.; Yu, L.; Chen, Y.; Hong, G. Degradable and excretable ultrasmall transition metal selenide nanodots for high-performance computed tomography bioimaging-guided photonic tumor nanomedicine in NIR-II bio-window. *Adv. Funct. Mater.* **2021**, *31*, 2008591.
- (4) Li, L.; Han, X.; Wang, M.; Li, C.; Jia, T.; Zhao, X. Recent advances in the development of near-infrared organic photothermal agents. *Chem. Eng. J.* **2021**, *417*, 128844.
- (5) Geng, B.; Qin, H.; Shen, W.; Li, P.; Fang, F.; Li, X.; Pan, D.; Shen, L. Carbon dot/WS₂ heterojunctions for NIR-II enhanced photothermal therapy of osteosarcoma and bone regeneration. *Chem. Eng. J.* **2020**, *383*, 123102.
- (6) Yang, N.; Gong, F.; Zhou, Y.; Hao, Y.; Dong, Z.; Lei, H.; Zhong, L.; Yang, X.; Wang, X.; Zhao, Y.; Liu, Z.; Cheng, L. A general in-situ reduction method to prepare core-shell liquid-metal/metal nanoparticles for photothermally enhanced catalytic cancer therapy. *Biomaterials* **2021**, *277*, 121125.
- (7) Gao, G.; Sun, X.; Liang, G. Nanoagent-promoted mild-temperature photothermal therapy for cancer treatment. *Adv. Funct. Mater.* **2021**, *31*, 2100738.
- (8) Wang, D.; Tang, M.; Jiang, H.; Li, M.; Jiang, S.; Sun, L.; Sun, J. Helical bowl-like SnS₂ with structure-induced conversion efficiency for enhanced photothermal therapy. *Chem. Eng. J.* **2020**, *400*, 125814.
- (9) Zhou, C.; Zhang, L.; Sun, T.; Zhang, Y.; Liu, Y.; Gong, M.; Xu, Z.; Du, M.; Liu, Y.; Liu, G.; Zhang, D. Activatable NIR-II plasmonic nanotheranostics for efficient photoacoustic imaging and photothermal cancer therapy. *Adv. Mater.* **2020**, *33*, 2006532.
- (10) Zhuang, Q.; Xu, J.; Deng, D.; Chao, T.; Li, J.; Zhang, R.; Peng, R.; Liu, Z. Bacteria-derived membrane vesicles to advance targeted photothermal tumor ablation. *Biomaterials* **2021**, *268*, 120550.
- (11) Chen, Y.; Gao, M.; Zhang, L.; Ha, E.; Hu, X.; Zou, R.; Yan, L.; Hu, J. Tumor microenvironment responsive biodegradable Fe-doped MoO_x nanowires for magnetic resonance imaging guided photothermal-enhanced chemodynamic synergistic antitumor therapy. *Adv. Healthcare Mater.* **2021**, *10*, e2001665.
- (12) Li, X.; Jiang, M.; Zeng, S.; Liu, H. Polydopamine coated multifunctional lanthanide theranostic agent for vascular malformation and tumor vessel imaging beyond 1500 nm and imaging-guided photothermal therapy. *Theranostics* **2019**, *9*, 3866–3878.
- (13) Wu, J.; Williams, G. R.; Zhu, Y.; Hu, T.; Wang, H.; Zhao, W.; Liang, R.; Weng, X.; Wei, M. Ultrathin chalcogenide nanosheets for photoacoustic imaging-guided synergistic photothermal/gas therapy. *Biomaterials* **2021**, *273*, 120807.
- (14) Xie, H.; Li, Z.; Sun, Z.; Shao, J.; Yu, X. F.; Guo, Z.; Wang, J.; Xiao, Q.; Wang, H.; Wang, Q. Q.; Zhang, H.; Chu, P. K. Metabolizable ultrathin Bi₂Se₃ nanosheets in imaging-guided photothermal therapy. *Small* **2016**, *12*, 4136–4145.
- (15) Cheng, Y.; Chang, Y.; Feng, Y.; Jian, H.; Tang, Z.; Zhang, H. Deep-level defect enhanced photothermal performance of bismuth sulfide-gold heterojunction nanorods for photothermal therapy of cancer guided by computed tomography imaging. *Angew. Chem., Int. Ed.* **2018**, *57*, 246–251.
- (16) Weng, Y.; Guan, S.; Wang, L.; Lu, H.; Meng, X.; Waterhouse, G. I. N.; Zhou, S. Defective porous carbon polyhedra decorated with copper nanoparticles for enhanced NIR-driven photothermal cancer therapy. *Small* **2019**, *16*, 1905184.
- (17) Wu, W.; Pu, Y.; Lu, X.; Lin, H.; Shi, J. Transitional metal-based noncatalytic medicine for tumor therapy. *Adv. Healthcare Mater.* **2021**, *10*, e2001819.
- (18) Chen, H.; Liu, T.; Su, Z.; Shang, L.; Wei, G. 2D transition metal dichalcogenide nanosheets for photo/thermo-based tumor imaging and therapy. *Nanoscale. Horizon* **2018**, *3*, 74–89.
- (19) Ma, N.; Zhang, M.-K.; Wang, X.-S.; Zhang, L.; Feng, J.; Zhang, X.-Z. NIR light-triggered degradable MoTe₂ nanosheets for combined photothermal and chemotherapy of cancer. *Adv. Funct. Mater.* **2018**, *28*, 1801139.
- (20) Wu, C.; Wang, S.; Zhao, J.; Liu, Y.; Zheng, Y.; Luo, Y.; Ye, C.; Huang, M.; Chen, H. Biodegradable Fe(III)@WS₂-PVP nanocapsules for redox reaction and TME-enhanced noncatalytic, photothermal, and chemotherapy. *Adv. Funct. Mater.* **2019**, *29*, 1901722.
- (21) Liu, S.; Pan, X.; Liu, H. Two-dimensional nanomaterials for photothermal therapy. *Angew. Chem., Int. Ed.* **2020**, *59*, 5890–5900.
- (22) Liu, M.; Zhu, H.; Wang, Y.; Sevcencan, C.; Li, B. L. Functionalized MoS₂-based nanomaterials for cancer phototherapy and other biomedical applications. *ACS Mater. Lett.* **2021**, *3*, 462–496.
- (23) Ma, H.; Xue, M. Recent advances in the photothermal applications of two-dimensional nanomaterials: photothermal therapy and beyond. *J. Mater. Chem. A* **2021**, *9*, 17569–17591.
- (24) Fan, R.; Chen, C.; Hou, H.; Chuan, D.; Mu, M.; Liu, Z.; Liang, R.; Guo, G.; Xu, J. Tumor acidity and near-infrared light responsive dual drug delivery polydopamine-based nanoparticles for chemo-photothermal therapy. *Adv. Funct. Mater.* **2021**, *31*, 2009733.
- (25) Yang, Y.; Zhao, R.; Zhang, T.; Zhao, K.; Xiao, P.; Ma, Y.; Ajayan, P. M.; Shi, G.; Chen, Y. Graphene-Based Standalone Solar

Energy Converter for Water Desalination and Purification. *ACS Nano* **2018**, *12*, 829–835.

(26) Luo, M.; Fan, T.; Zhou, Y.; Zhang, H.; Mei, L. 2D black phosphorus-based biomedical applications. *Adv. Funct. Mater.* **2019**, *29*, 1808306.

(27) Yang, X.; Wu, R.; Xu, N.; Li, X.; Dong, N.; Ling, G.; Liu, Y.; Zhang, P. Application and prospect of antimonene: A new two-dimensional nanomaterial in cancer theranostics. *J. Inorg. Biochem.* **2020**, *212*, 111232.

(28) Huang, Y.; Zhao, Y.; Liu, Y.; Ye, R.; Chen, L.; Bai, G.; Xu, S. Erbium-doped tungsten selenide nanosheets with near-infrared II emission and photothermal conversion. *Chem. Eng. J.* **2021**, *411*, 128610.

(29) Huang, Y.; Bai, G.; Zhao, Y.; Liu, Y.; Xu, S.; Hao, J. Lanthanide-doped topological nanosheets with enhanced near-infrared photothermal performance for energy conversion. *ACS Appl. Mater. Interfaces* **2021**, *13*, 43094–43103.

(30) Huang, Y.; Zhao, Y.; Liu, Y.; Xu, B.; Xu, S.; Bai, G. Lanthanide doped two dimensional heterostructure nanosheets with highly efficient harvest towards solar energy. *Mater. Des.* **2021**, *210*, 110023.